Earth and Planetary Science Letters 442 (2016) 143–156

Contents lists available at ScienceDirect

Earth and Planetary Science Letters

www.elsevier.com/locate/epsl

Frequency modulation reveals the phasing of orbital eccentricity during Cretaceous Oceanic Anoxic Event II and the Eocene hyperthermals

Jiří Laurin [a,*], Stephen R. Meyers [b], Simone Galeotti [c], Luca Lanci [c]

[a] Institute of Geophysics, Academy of Sciences of the Czech Republic, Boční II/1401, Praha 4, Czech Republic
[b] University of Wisconsin – Madison, Department of Geoscience, 1215 W. Dayton St., Madison, WI 53706, USA
[c] Department of Pure and Applied Science, University of Urbino "Carlo Bò", 61029 Urbino (PU), Italy

ARTICLE INFO

Article history:
Received 4 August 2015
Received in revised form 23 February 2016
Accepted 25 February 2016
Available online xxxx
Editor: D. Vance

Keywords:
orbital eccentricity
cyclostratigraphy
Cenomanian
black shale
Eocene
hyperthermal

ABSTRACT

Major advances in our understanding of paleoclimate change derive from a precise reconstruction of the periods, amplitudes and phases of the 'Milankovitch cycles' of precession, obliquity and eccentricity. While numerous quantitative approaches exist for the identification of these astronomical cycles in stratigraphic data, limitations in radioisotopic dating, and instability of the theoretical astronomical solutions beyond ~50 Myr ago, can challenge identification of the phase relationships needed to constrain climate response and anchor floating astrochronologies. Here we demonstrate that interference patterns accompanying frequency modulation (FM) of short eccentricity provide a robust basis for identifying the phase of long eccentricity forcing in stratigraphic data. One- and two-dimensional models of sedimentary distortion of the astronomical signal are used to evaluate the veracity of the FM method, and indicate that pristine eccentricity FM can be readily distinguished in paleo-records. Apart from paleoclimatic implications, the FM approach provides a quantitative technique for testing and calibrating theoretical astronomical solutions, and for refining chronologies for the deep past.

We present two case studies that use the FM approach to evaluate major carbon-cycle perturbations of the Eocene and Late Cretaceous. Interference patterns in the short-eccentricity band reveal that Eocene hyperthermals ETM2 ('Elmo'), H2, I1 and ETM3 (X; ~52–54 Myr ago) were associated with maxima in the 405-kyr cycle of orbital eccentricity. The same eccentricity configuration favored regional anoxic episodes in the Mediterranean during the Middle and Late Cenomanian (~94.5–97 Myr ago). The initial phase of the global Oceanic Anoxic Event II (OAE II; ~93.9–94.5 Myr ago) coincides with maximum and falling 405-kyr eccentricity, and the recovery phase occurs during minimum and rising 405-kyr eccentricity. On a Myr scale, the event overlaps with a node in eccentricity amplitudes. Both studies underscore the importance of seasonality in pacing major climatic perturbations during greenhouse times.

1. Introduction

Earth's astronomical parameters control the seasonal and latitudinal distribution of solar radiation entering the Earth's atmosphere, following the periodicities of axial precession (c. 20 kyr), axial obliquity (c. 40 kyr) and orbital eccentricity (95–124 and 405 kyr; e.g., Berger et al., 1993; Laskar et al., 1993). Attempts to reconstruct the underlying mechanisms of climate forcing – such as glacial/interglacial cyclicity or monsoonal variations – have relied strongly on detailed quantification of the phase of these astronomical parameters as they relate to observed climate events (e.g., Hays et al., 1976; Ruddiman, 2006). Ultimately, the phases of the precessional and obliquity cycles, and their longer modulating terms (e.g., eccentricity), influence the amplitude of seasonality variations (e.g., Berger et al., 1993; Laskar et al., 1993). The possibility of correlating the onsets and terminations of climate events to the intensity of seasonality is often a key step towards understanding the causal mechanisms of paleoclimate change (e.g., Imbrie et al., 1993; Lourens et al., 2005; Lunt et al., 2011).

The importance of reconstructing the amplitudes and phases of astronomical parameters from the geologic record has increased following the discovery of very-long term (Myr- and multi-Myr-scale) astronomical influences on past climate (e.g., Herbert, 1997; Pälike et al., 2006; Valero et al., 2014; Wendler et al., 2014; Laurin et al., 2015), which are attributed to the amplitude modulation (AM) of Milankovitch terms. While the existence of these

* Corresponding author.
E-mail address: laurin@ig.cas.cz (J. Laurin).

http://dx.doi.org/10.1016/j.epsl.2016.02.047
0012-821X/

short- and long-term cycles is well established, the phasing is often uncertain (e.g., discussions in Laurin et al., 2014, 2015), resulting in ambiguity about the specific climate forcing mechanisms involved. The present study introduces a new approach for determining the phase of astronomical forcing preserved in strata, based on interference patterns (constructive and destructive interference of cycles) associated with frequency modulation (FM). Following validation of the approach with a series of one- and two-dimensional stratigraphic models, the technique is applied to evaluate major perturbations to the global carbon cycle associated with Cretaceous Oceanic Anoxic Event II (Schlanger and Jenkyns, 1976) and the Eocene hyperthermals (e.g., Lourens et al., 2005; Galeotti et al., 2010; Zachos et al., 2010). In both case studies, the results unambiguously identify the phasing of 405-kyr eccentricity forcing (and thus the amplitude of seasonality variation), and provide important constraints for anchoring the floating time scales to the theoretical astronomical solutions.

2. Background

2.1. Common approaches for determining the phase of astronomical forcing

A number of techniques are commonly used to identify the phase of astronomical forcing from paleoclimate data. These include attempts to directly correlate observed sedimentary rhythms with the theoretical astronomical solutions (Laskar et al., 2004, 2011a, 2011b), often times involving quantitative analysis of AM of lithological or geochemical parameters attributed to astronomical signals (e.g., Lourens et al., 2005; Herbert et al., 1999; Mitchell et al., 2008; Galeotti et al., 2010). However, interpretation of phase by direct comparison of stratigraphic data to the theoretical solutions is often challenged by radioisotopic constraints, which generally exceed the temporal wavelength of the astronomical parameters. In addition to this factor, the chaotic behavior of the Solar System yields instabilities in the theoretical solutions beyond ~50 Myr ago, making it difficult to constrain the phase of insolation beyond the Eocene (Laskar et al., 2011a, 2011b; Westerhold et al., 2012; notable exception to this is the 405-kyr eccentricity cycle, which is predicted to be remarkably stable throughout the Phanerozoic; Laskar et al., 2004, 2011a, 2011b). These challenges notwithstanding, assessment of precession AM and short eccentricity AM in paleoclimate data provides the potential to constrain the phase relationship between climate forcing and response at the eccentricity scale (e.g., Hilgen, 1991; Lourens et al., 2005).

Modulations of precessional index and short eccentricity are inherently tied to the phase of short eccentricity and long eccentricity, respectively (Fig. 1). Thus, a theoretically well-founded basis for astronomical phase evaluation exists, through assessment of the recurrence and intensity of distinct lithologies (e.g., Herbert et al., 1999; Lourens et al., 2005; Batenburg et al., 2016), bandpass filtering of inferred astronomical signals (e.g., Lourens et al., 2005; Mitchell et al., 2008; Wu et al., 2013), and complex demodulation (e.g., Shackleton et al., 1995). A difficulty, however, arises when applying the theoretical template (Fig. 1) to real stratigraphic records, which respond to a multitude of depositional, diagenetic and climatic influences (Meyers et al., 2008). Stochastic or systematic noise introduced into the sedimentary record can fabricate an artificial AM in a bandpassed signal (Fig. 2; Huybers and Aharonson, 2010), and with an increase in the noise to signal ratio AM of the bandpassed signal becomes increasingly sensitive to the selection of filter window and bandwidth (Fig. 2b). In point of fact, new astrochronologic testing approaches have been introduced that specifically address and resolve the problem of artificially generated AM (Zeeden et al., 2015; Meyers, 2015). However, given common practice filtering approaches in cyclostratigraphy (e.g., relatively narrow bandpass filters; see Zeeden et al., 2015) and plausible noise and distortions – such as astronomical-scale fluctuations in sedimentation rate and diagenesis – phase assessment can be severly compromised (e.g., Figs. 3, 4 and S1.1; see Section 4.1 for more examples). AM can also be affected by the sampling strategy (Fig. S1.2), non-linearities inherent to the sedimentary response to climate change (e.g., Laurin et al., 2005), variations in depositional and/or climatic thresholds and amplitude leakage induced by, for example, bioturbation (Ripepe and Fischer, 1991) or inertia of the system (e.g., the effect of residence time of carbon in the ocean–atmosphere system). The attribution of AM to the original astronomical forcing therefore requires tools that would help to distinguish pristine modulation patterns from artifacts (see also Zeeden et al., 2015 and Meyers, 2015). Below we demonstrate that such a tool can be found in the interference patterns accompanying FM of astronomical signals, which are revealed by 'evolutive' or 'sliding-window' spectral techniques.

2.2. An alternative approach for determining the phase of astronomical forcing: frequency modulation of the eccentricity signal

Earlier studies (Herbert, 1992; Hinnov and Park, 1998; Hinnov, 2000 and references therein) have recognized that FM and its phase relationship to AM can provide critical information about astronomically forced variability in depositional conditions. Furthermore, changes in spatial (depth-domain) frequency modulation are now being routinely used to identify sedimentation-rate changes (e.g., Meyers et al., 2001) and hiatuses (Meyers and Sageman, 2004) in strata. However, little attention has been paid to the application of FM to identify the phase of astronomical forcing (although see Rial, 1999). We focus on the modulation of orbital eccentricity, which forms a relatively long-term astronomical control and as such can be readily examined even in slowly accumulating pelagic and hemipelagic strata. The approach developed here, however, is also applicable to shorter term precession cycles, with stronger requirements on the sampling resolution.

The principal changes in the eccentricity of Earth's orbit are related to gravitational perturbations from Venus (g_2), Mars (g_4), and Jupiter (g_5), and occur with periods of 405 kyr (g_2–g_5), 124 kyr (g_4–g_2), and 95 kyr (g_4–g_5; where g_2, g_4 and g_5 are fundamental frequencies of the secular system; Laskar et al., 2004; see also Hinnov, 2000). These three principal terms are respectively labeled E1, E2 and E3 in this paper. The E2 and E3 variations are themselves composed of a series of closely spaced harmonic components, the most prominent of which have periods of 133.8, 131.3, 127.2, 124.6, 100.4, 99.3, 96.6 and 95.2 kyr (solution La2011, interval 80–100 Myr ago). Frequency spectra of real stratigraphic records are, however, averaged across a broader frequency band, so the short-eccentricity terms identified in stratigraphic data should be close to 124 kyr and 95 kyr. The ratio of E1 vs. E2 and E3 periods is considered stable within ±5% throughout the Phanerozoic (3.19 ± 0.17 and 4.19 ± 0.17, respectively; Waltham, 2015).

As illustrated in Fig. 1, the E1 term appears both as a distinct cycle in the frequency domain and as a frequency modulation of the E2 and E3 cycles in the theoretical solution. The E1 eccentricity maxima are accompanied by a constructive interference of E2 and E3, which give rise to a high-amplitude response in the bulk eccentricity signal (Fig. 1a) with a single frequency maximum approximately halfway between the frequencies of E2 and E3 (~9 cycle/Myr, arrows in Fig. 1e). In contrast, eccentricity minima of the E1 signal are linked to a destructive interference of the E2 and E3 terms, which produce a muted ~100-kyr variance in the bulk eccentricity signal, and are expressed as a distinct split into the E2 and E3 signals in the frequency domain (Fig. 1). Hence, given an adequately preserved eccentricity signal, maxima

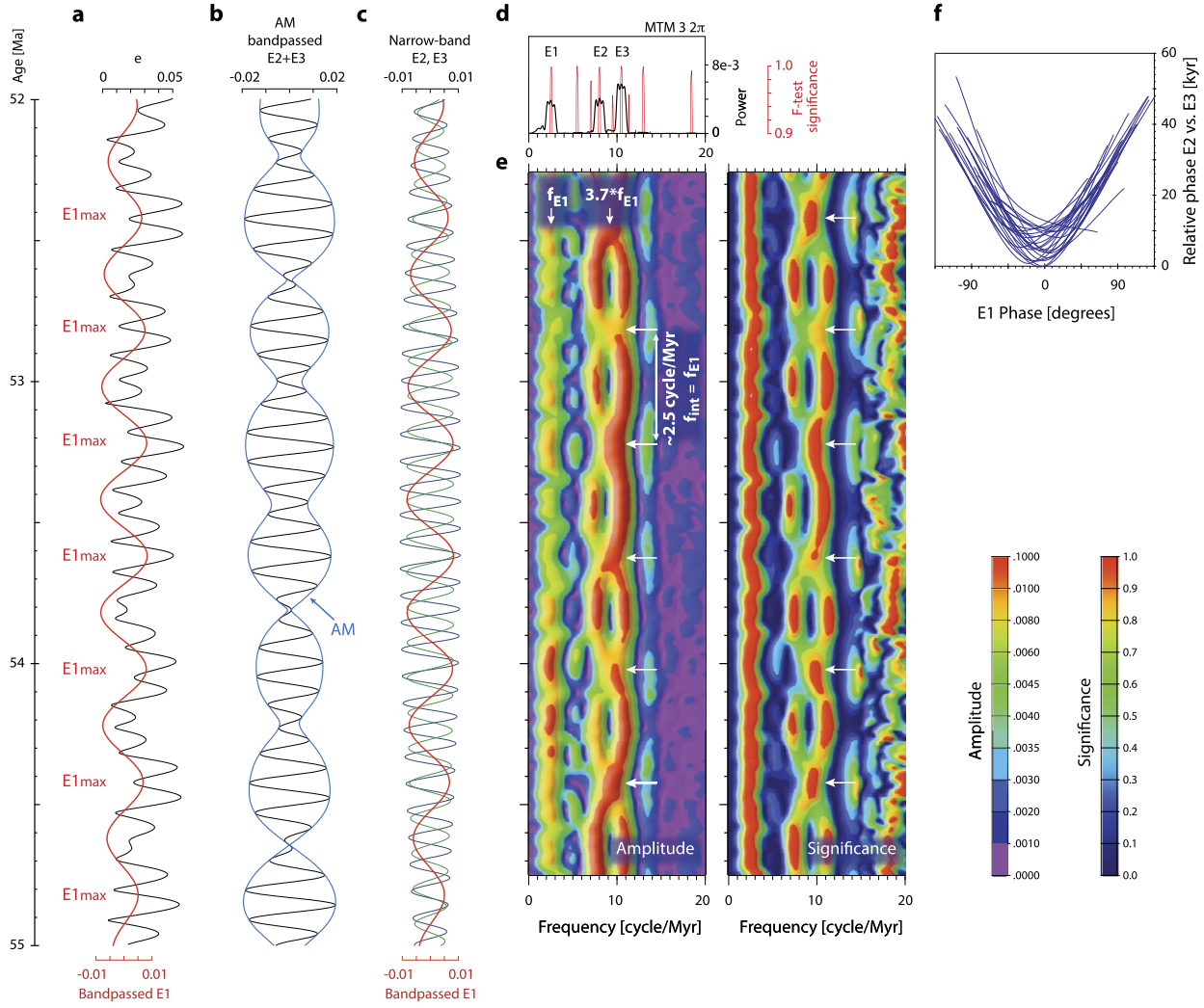

Fig. 1. Modulation and phasing of orbital eccentricity. **(a)** Eccentricity (e; solution La2011, 52–55 Myr ago). Bandpassed 405-kyr term (E1; 2.5 ± 0.3 cycle/Myr, Gaussian filter) is shown in red. E1 max = 405-kyr eccentricity maximum. **(b)** Amplitude modulation (AM) of short eccentricity (E2 + E3; 9.5 ± 3.0 cycle/Myr, Gaussian filter). AM is commonly used as a tool to identify the phase of eccentricity forcing in stratigraphic records. Here we propose that the analysis of AM should be combined with an examination of frequency modulation (FM) and interference patterns that are tightly linked to the phase of the modulating cycle as shown further below: **(c)** Phasing of the main eccentricity components. Narrow-band filtered E2 (125 kyr; 8.0 ± 0.3 cycle/Myr, Gaussian filter) in green, and E3 (95 kyr; 10.5 ± 0.3 cycle/Myr, Gaussian filter) in black. Note that E2 and E3 interfere constructively at E1 max (bandpassed E1 in red; 2.5 ± 0.3 cycle/Myr, Gaussian filter). **(d)** MTM power spectrum and F-test significance for eccentricity. **(e)** Evolutive Harmonic Analysis (EHA; Meyers et al., 2001) amplitude and F-test significance spectra (MTM 3 2π; 500-kyr window). White arrows mark intervals of constructive interference ('junctions') of E2 and E3 beats that form at 405-kyr eccentricity maxima. Note that the mean frequency of the interfering components (E2 and E3) is the 3.7-th multiple of the recurrence frequency of the interference patterns ($f_{int} \sim 2.5$ cycle/Myr); this ratio serves as a diagnostic feature of pristine eccentricity modulation (see text). **(f)** Scatter plot documenting the relationship between the relative phasing of E2 vs. E3 (vertical axis) and the phase of 405-kyr cycle. Note that the E2 and E3 cycles are in phase (i.e., interfere constructively) at 405-kyr maxima (0 deg. phase of E1). (For interpretation of the references to color in this figure legend, the reader is referred to the web version of this article.)

and minima in E1 eccentricity can be traced by a systematic FM and associated interference patterns in the E2–E3 band (Fig. 1e); these patterns can serve as a tool for the recognition of E1 phasing in paleo-records.

The ratio of interfering (E2 + E3) and modulating (E1) signals is defined by the theoretical orbital solutions (e.g., La2011; Laskar et al., 2011b), thus the above relationships can be summarized with the following equation (using the example of E1 modulation of E2 + E3):

$$p_{int} = p_{E1} = \left[(p_{E2} + p_{E3})/2\right] * R \quad (1)$$

where p_{int} is the spatial period, or recurrence interval of the interference features, p_{E1} is the spatial period of the E1 signal, p_{E2} and p_{E3} are spatial periods of the E2 and E3 signals, respectively, and R is the ratio of the E1 period vs. mean E2–E3 period in the orbital solution La2011 ($R = 3.7 \pm 0.2$ for the Phanerozoic; cf. Waltham, 2015). In the frequency domain, the equation (1) becomes

$$f_{int} = f_{E1} = \left[(f_{E2} + f_{E3})/2\right]/R \quad (2)$$

where f_{int} is the spatial frequency of the interference features, f_{E1} is the spatial frequency of the E1 signal, and f_{E2} and f_{E3} are spatial frequencies of the E2 and E3 signals, respectively (see Fig. 1).

Before applying this tool to real stratigraphic series, however, it is necessary to evaluate the sensitivity of FM to distortions arising from the climate and depositional system transfer functions (Meyers et al., 2008). Most importantly, it is essential to show that processes accompanying orbital signal transfer to the sedimentary record cannot fabricate false patterns that could be misinterpreted as FM of the original forcing. The effects of sedimentation rate changes, differential compaction, diagenetic carbonate redistribution and undersampling are examined in Section 4, with one- and two-dimensional numerical models of orbitally driven sedimenta-

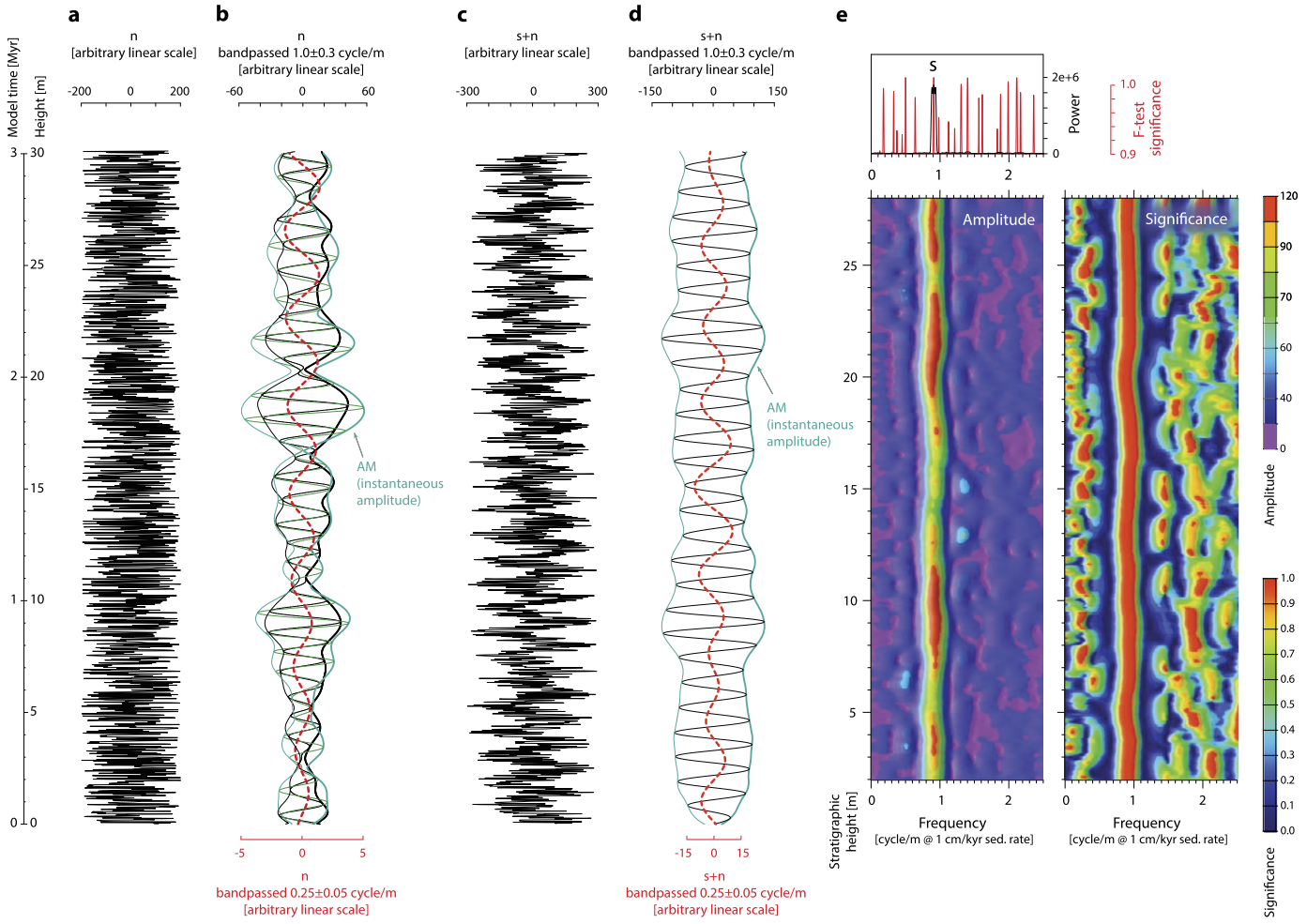

Fig. 2. Limitations of the conventional AM approach to phase interpretation. **(a)** Time series consisting of a white noise. Sedimentation rate 1 cm/kyr. Model #1, Table S1. **(b)** White noise filtered in the expected short-eccentricity band. Black lines: Gaussian filter, 1.0 ± 0.3 cycle/m. Green lines: rectangular filter, 1.0 ± 0.3 cycle/m. Dashed red line denotes white noise filtered in the 405-kyr band (Gaussian filter, 0.25 ± 0.05 cycle/m). Note a well-defined AM, which locally resembles the 405-kyr bundling of short-eccentricity cycles. This AM is an artifact of filtering across a ± 0.3 cycle/m bandwidth. **(c)** Time series consisting of a sinusoidal, 110-kyr signal (s) and white noise (n). Model #2, Table S1. **(d)** Time series s + n filtered in the short-eccentricity band (Gaussian filter, 1.0 ± 0.3 cycle/m). Dashed red line: Gaussian filter, 0.25 ± 0.05 cycle/m. The inclusion of noise generates artificial AM that resembles eccentricity bundling in places (e.g., intervals 7–11, or 19–24 m). The conventional AM approach cannot distinguish these types of signal distortion, thus potentially misinterpreting the artificial AM as a signature of 405-kyr modulation (see also Zeeden et al., 2015 and Meyers, 2015). **(e)** Spectral estimates for the series s + n: MTM (3 2π) power spectral and significance estimates for the entire series (top), and EHA (MTM 3 2π) amplitude and significance, 4-m moving window. Minor frequency slips are present. However, the artificial AM is not associated with systematic FM and interference patterns that characterize real astronomical signals (compare with Fig. 1). (For interpretation of the references to color in this figure legend, the reader is referred to the web version of this article.)

tion. These models demonstrate that FM is generally a resilient tool for reconstructing the phase of the 405-kyr eccentricity cycle.

3. Material and methods

3.1. Theoretical astronomical solutions

All stratigraphic models discussed in this paper are based on the astronomical solutions La2010d (Laskar et al., 2011a) and La2011 (Laskar et al. 2011b). La2010d is a *full solution* that allows reconstructions of eccentricity, obliquity and precession (see appendix of Wu et al., 2013). The required numerical constraints for calculation of La2011-equivalent precession and obliquity are currently not available; the latest solution La2011 is therefore used only in models with an imposed eccentricity forcing (no precession). The stratigraphic data sets from the Eocene and Cretaceous are compared with orbital eccentricity from La2011 (Laskar et al. 2011b), which is currently considered the most stable solution for these intervals (Westerhold et al., 2012).

3.2. Stratigraphic models of astronomical forcing

To test the preservation potential of FM patterns following depositional and post-depositional processes, we develop 7 suites of simple one-dimensional models and one suite of two-dimensional models (30 individual models in total) that simulate astronomically paced changes in sedimentary (lithological or geochemical) parameters. Our focus is on depositional and post-depositional distortions that follow the same rhythm as precessional and eccentricity variations, because these distortions can fabricate false modulation patterns that are most easily confused for pristine astronomical AM and FM. The simplest examples apply constant sedimentation rates (Figs. S1.2 and S1.8). The effect of changing sedimentation rates is examined with one-dimensional models in which the net sedimentation rate (averaged over 5-kyr time steps) is linearly (Figs. 3, S1.1, S1.3 and S1.4) or non-linearly (Figs. S1.6, S1.7, S1.9 and S1.10) proportional to the astronomical forcing. Both positive and negative relationships between the astronomical forcing and sedimentation rate are modeled. In one group of models (Fig. S1.4) the sedimentation rate is allowed to decrease to 0 cm/kyr at

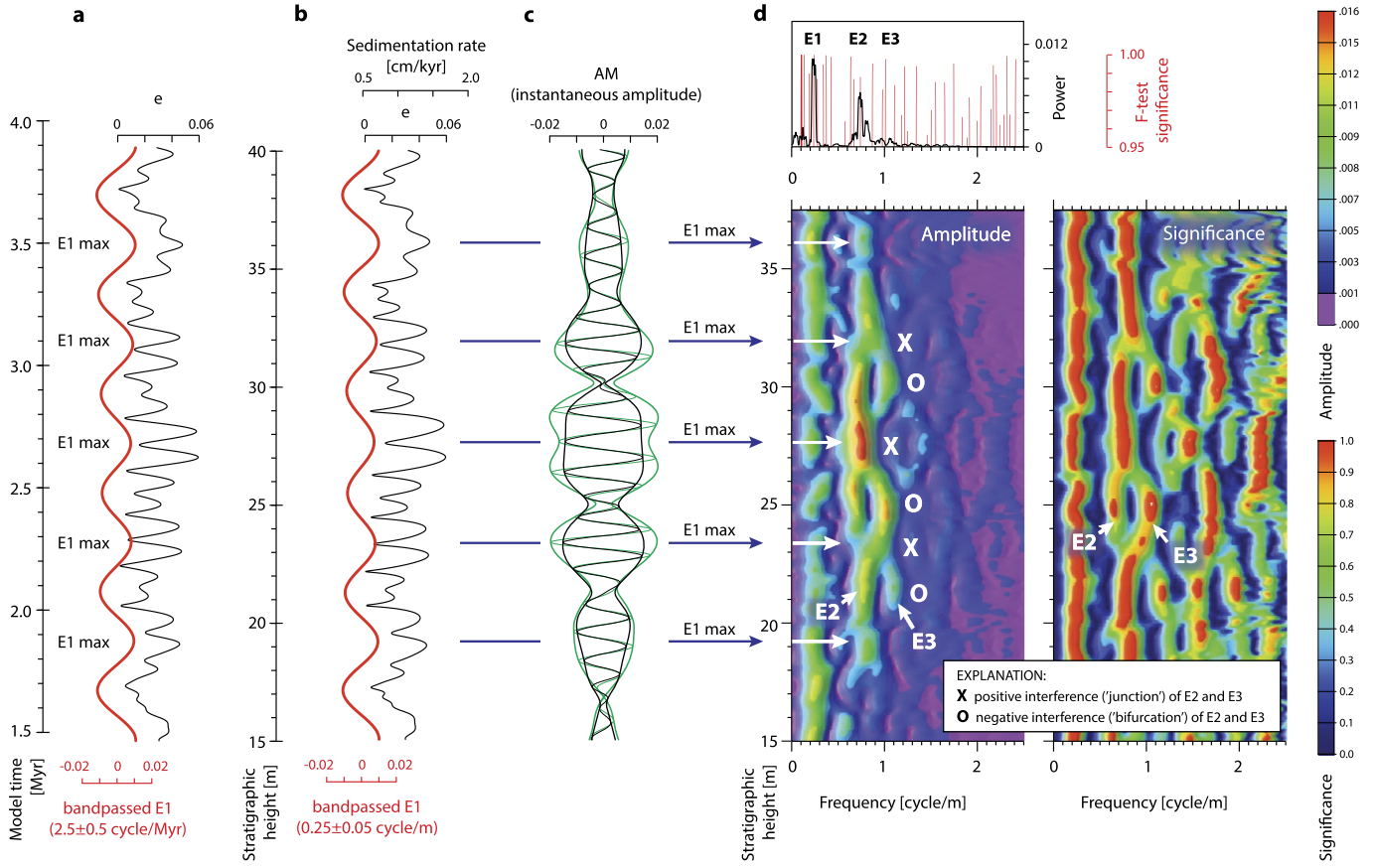

Fig. 3. Preservation and distortion of E2–E3 interference. In this model (#4, Table S1), sedimentation rate is linearly proportional to orbital eccentricity. **(a)** Orbital eccentricity (e; solution La2010d, interval 96–98.5 Ma) plotted against time. Bandpassed 405-kyr eccentricity shown in red (2.5 ± 0.5 cycle/Myr, Gaussian filter). E1 max = 405-kyr maximum. **(b)** Orbital eccentricity and sedimentation rate plotted against stratigraphic height. Bandpassed 405-kyr eccentricity shown in red (0.25 ± 0.05 cycle/m, Gaussian filter). **(c)** AM of the E2 + E3 signal in e (0.9 ± 0.3 cycle/m). AM is generally sensitive to the selection of filter parameters (black line: Gaussian filter; green line: rectangular filter), and provides an unstable basis for the interpretation of E1 maxima and minima (see also Figs. 2, 4d, and 5c). The record of FM in time-frequency plots makes it possible to identify distortion: **(d)** Spectral estimates for the parameter e in the depth domain: MTM ($3\ 2\pi$) power spectral and significance estimates for the entire series (top), and EHA (MTM $3\ 2\pi$) amplitude and significance, 5-m moving window. Eccentricity terms E1, E2 and E3 are indicated. Note that 'junctions' (X) and 'bifurcations' (O) originating from the interference of E2 and E3 identify the source of AM and thus facilitate a correct interpretation of the 405-kyr maxima and minima in the orbital forcing. See also Fig. S1.1. (For interpretation of the references to color in this figure legend, the reader is referred to the web version of this article.)

certain orbital configurations to simulate the effect of hiatuses. A strongly non-linear forcing of sedimentation rate (Figs. S1.6 and S1.7) is also considered to mimic a differential compaction of layers deposited during different phases of the astronomical cycle. Carbonate redistribution between mud-dominated and carbonate-dominated lithologies would have a similar effect. Selected models are tested for artifacts introduced by different sampling strategies and undersampling (Figs. S1.2 and S1.5). These models explore both imposed eccentricity signals (Figs. 3, 4, 5, S1.1, and S1.8 through S1.11) and eccentricity signals originating from a nonlinear transformation of the precessional cycle (Figs. S1.2 through S1.7). Distortions imparted to nearshore and dilution-driven hemipelagic strata by the transfer of astronomical signal via sea-level change (Laurin et al., 2005) are examined with a two-dimensional numerical model (selected output data are shown in Figs. 5 and S1.11).

Parameters of the one-dimensional models are described and illustrated in Table S1 and Figs. 3, 4, and S1. Two-dimensional stratigraphic models were executed with the modeling software "SedTec2000" (Boylan et al., 2002) and are similar in their setup to the "MILex" model of Laurin et al. (2005; for details see Data Repository Items accompanying this paper) with the following differences: (1) length of the model run is 4 Myr, (2) model time step is 2 kyr, and (3) the sea level curve is calculated from the solution La2010d using the following formula: $SL = e * a + e1 * b$, where e is eccentricity, $e1$ is the bandpassed 405-kyr eccentricity term (Gaussian filter, 2.5 ± 0.5 cycle/Myr), a and b are multipliers (see Table S2). FM patterns were examined on a simulated depth-domain series of the percentage of fine-grained siliciclastics sampled 100 km from the model basin margin.

3.3. Floating astrochronology development for paleo-records (Cretaceous and Eocene), and time series analysis approaches

Spectral estimates for the stratigraphic data and model results are calculated with the multitaper method (MTM; Thomson, 1982) using evolutive harmonic analysis (EHA; Meyers et al., 2001). The statistical significance of the EHA spectral results are quantified using the MTM harmonic F-test (for phase-coherent sinusoids; Thomson, 1982). To conduct astrochronologic testing and comprehensively evaluate a range of plausible sedimentation models for the Eocene and Cretaceous data sets, Evolutive Average Spectral Misfit (E-ASM; Meyers and Sageman, 2007; Meyers, 2014) is implemented. This permits an objective and comprehensive test of published astronomical interpretations for the Cretaceous and Eocene data (Lanci et al., 2010; Galeotti et al., 2010), and simultaneously, evaluation of changes in sedimentation rate throughout the study intervals. Unless otherwise indicated, all analyses use three tapers and a time-bandwidth product of 2. The preferred EHA window size for the analysis of E2–E3 interference is 5x the spatial period of the proposed E2–E3 signal.

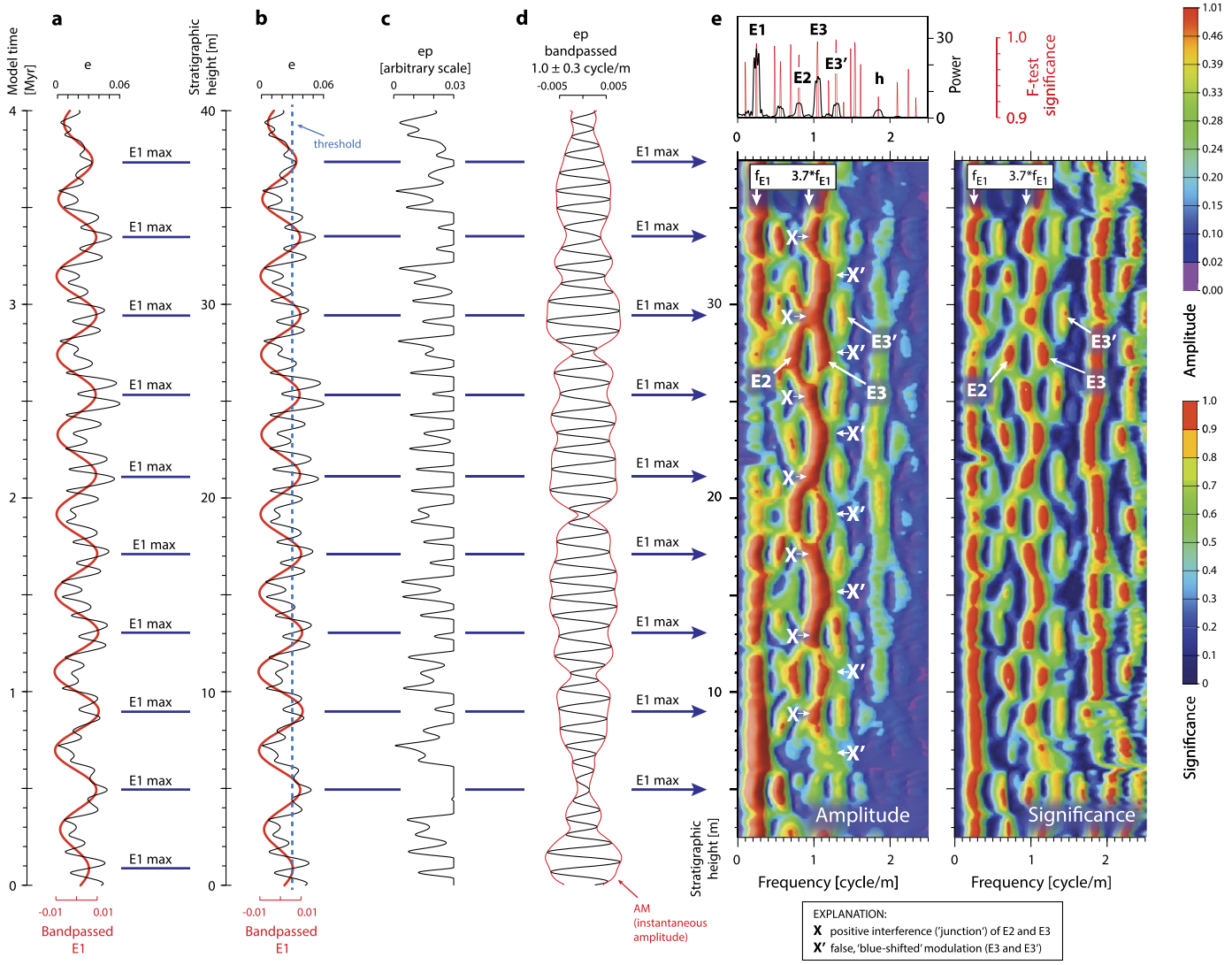

Fig. 4. Preservation and distortion of E2–E3 interference. This model (#22, Table S1) uses a constant sedimentation rate (1 cm/kyr) and a non-linear (reversely clipped) response of sedimentary proxy (ep) to orbital eccentricity (e). **(a)** Model input; La2010d solution for eccentricity, interval 93–97 Myr ago, plotted against time. **(b)** Model input plotted against stratigraphic height. **(c)** A non-linear proxy of orbital eccentricity plotted against stratigraphic height. This proxy is modeled as proportional to orbital eccentricity, but only for eccentricity values below 0.03, i.e., the proxy is considered insensitive to eccentricity maxima. **(d)** Parameter ep filtered in the E2–E3 band (1.0 ± 0.3 cycle/m, Gaussian filter). Note that AM of the E2–E3 signal is strongly distorted, and does not trace the maxima and minima in 405-kyr (E1) eccentricity. **(e)** Spectral estimates for the parameter ep: MTM ($3\ 2\pi$) power spectral and significance estimates for the entire series (top), and EHA (MTM $3\ 2\pi$) amplitude and significance, 5-m moving window. Eccentricity terms E1, E2 and E3 are indicated; h = harmonic noise. Intervals of constructive interference of the E2 and E3 signals are marked with X. These primary FM patters are centered at the 3.7-th multiple of the E1 frequency (f_{E1}) and trace closely the maxima in the E1 cycle (E1 max). With an increasing distortion, the E2 signal fades and the variance is transferred towards a new spectral maximum E3′ (see also Fig. 5). This change gives rise to secondary modulation patterns (X′) that may resemble the original FM, but are out-of-phase from E1 maxima. The apparent 'blue shift' of the X′ modulations relative to the $3.7 * f_{E1}$ frequency can serve as a diagnostic feature distinguishing pristine modulation from artifacts. (For interpretation of the references to color in this figure legend, the reader is referred to the web version of this article.)

Preparation of the Cretaceous IRM (Lanci et al., 2010) and Eocene $CaCO_3$ (Galeotti et al., 2010) data involve resampling on an evenly-spaced grid by piecewise linear interpolation (10 cm for the IRM data and 3 cm for the $CaCO_3$ data; these values meet or exceed the median sampling interval). All analyses are conducted using the *R* package 'Astrochron' (Meyers, 2014; R Core Team, 2015).

4. Results and discussion

4.1. Stratigraphic modeling results: depositional distortions of frequency modulation

The stratigraphic modeling studies indicate that original interference patterns of eccentricity FM are resistant to simple sedimentary distortions, including 20–100% sedimentation-rate changes that are positively or negatively proportional to the precessional and eccentricity forcing. Unlike AM, the interference patterns appear relatively insensitive to undersampling (Figs. S1.2 and S1.5). As regards destabilization of the primary FM, imposed eccentricity variations in sedimentation rate are generally more efficient than precession-paced changes, since the size of the moving window permits averaging across many precessional cycles. A greater distortion is also observed in model setups that employ a non-linear threshold response of sedimentation rate (or differential compaction) and, in particular, when assuming a threshold response for both sedimentation rate and the sedimentary proxy of astronomical variations (Figs. S1.6 and S1.7).

False interference patterns similar to those of the original signal often form in parts of the distorted record. Importantly, however, in all instances encountered in the one- and two-dimensional

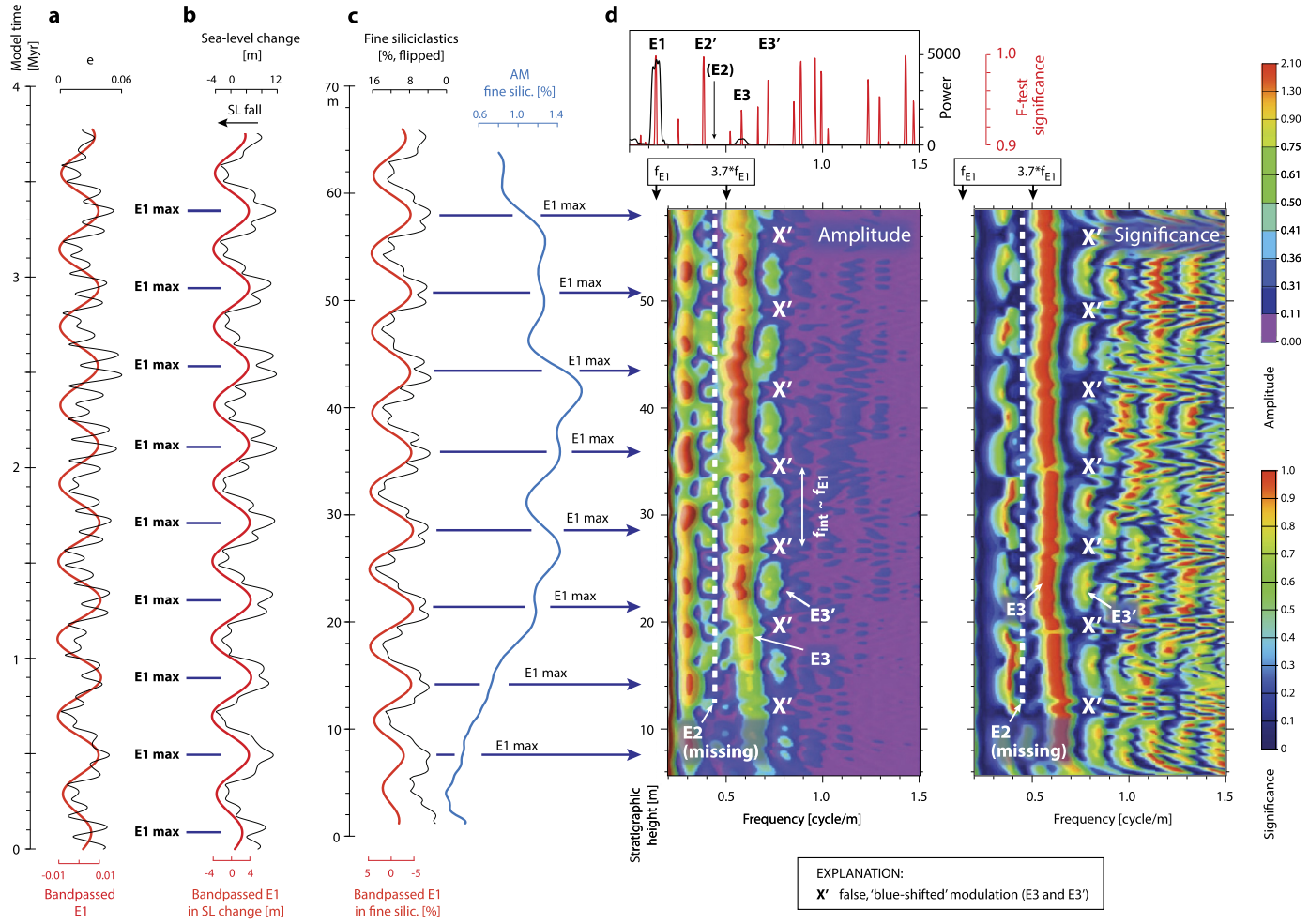

Fig. 5. Distortion of E2–E3 interference. An example from two-dimensional stratigraphic modeling (run #32; Tab. S2). **(a)** La2010d solution for eccentricity (e), interval 93–97 Ma, plotted against time. **(b)** Eccentricity-paced sea-level fluctuations obtained by imposing a 405-kyr component upon bulk eccentricity (see Table S2 for details). **(c)** Selected model output: proportion of fine siliciclastics in dilution-driven hemipelagic strata. AM of the short-eccentricity signal is shown in blue (0.6 ± 0.1 cycle/m, Gaussian filter, Hilbert transformed). **(d)** Spectral estimates for the parameter shown in c: MTM ($3\ 2\pi$) power spectral and significance estimates for the entire series (top), and EHA (MTM $3\ 2\pi$) amplitude and significance, 10-m moving window. E2′ and E3′ refer to distorted ('red' or 'blue' shifted) frequencies of E2 and E3. Symbols X′ refer to artificial modulations that follow the same rhythm as the E1 signal ($f_{\text{int}} \sim f_{\text{E1}}$), but are phase shifted relative to E1 maxima (the origin of this phase-lagged modulation is explained in Laurin et al., 2005). The key diagnostic feature of the distorted FM patterns is the 'blue shift' of the interfering frequencies relative to the $3.7 * f_{\text{E1}}$ frequency. (For interpretation of the references to color in this figure legend, the reader is referred to the web version of this article.)

models these artifacts either eradicate the strong correlation with the (bandpassed) E1 rhythm, or occur at 'red-' or 'blue-shifted' frequencies. Their recurrence interval is often much longer than the original pacing (Figs. S1.6 and S1.7), which makes them readily recognizable in paleo-data. Somewhat counter intuitively, distorted E2–E3 signals appear more stable in some intervals, as they lack the frequent bifurcations at E1 minima (Fig. S1.6; see also Fig. 5). Other features of the distorted signals include shifting of the interfering frequencies by 5–30% towards or away from the original E2–E3 frequencies (Figs. 4, 5, and S1.6 through S1.11) and the formation of harmonic noise at multiples or divisors of the E2–E3 frequencies (e.g., Figs. 4, S1.2 and S1.6). As discussed below, when such distortions (lack of bifurcations, 'blue/red shift') are observed in paleo-data, they can be used as diagnostics to identify such records as unsuitable for phase assessment.

4.2. Stratigraphic modeling results: FM interference patterns as a tool and feedback in phase interpretation

Evaluation of the above stratigraphic models suggests that pristine FM patterns can often survive common sedimentary distortions. Stronger distortions accompanying pronounced differential compaction, non-linear fluctuations in sedimentation rate and/or strongly non-linear responses of sedimentary proxies to astronomical forcing can destroy the original patterns and create false, artificial interference features. These artifacts can, however, be readily identified in paleo-data. Thus, confirmation of a primary origin of the FM can be guided by the following features: (1) the recurrence interval of the interference patterns revealed by time-frequency analysis should be identical (within the limits of spectral resolution) with the E1 recurrence interval prescribed in equation (1), (2) the interference should occur in the frequency band of the primary interfering signals (E2 and E3), and therefore lack a 'red-' or 'blue-shifted' distortion in excess of the uncertainty in the parameter R (equations (1) and (2); Figs. 4, 5, and S1.6 through S1.11), and (3) if E1 variance is present in the data series (in addition to its modulation of E2 + E3), the recurrence interval of the interference patterns should be in rhythm with the bandpassed E1 signal. Importantly, these relationships are applicable for the evaluation of "untuned" spatial data, and do not require preservation and detection of the modulating signal (E1 in this case). AM and FM patterns not meeting the above criteria should *a priori* be considered distorted and caution should be exercised when attempting to interpret the specific phase of orbital signals, although these

records may still be valuable for developing floating astrochronologies and for the interpretation of depositional system response to orbital forcing (e.g., Laurin et al., 2005).

Therefore, based on these modeling results we propose that interference patterns can be used as a tool to interpret the phasing of 405-kyr eccentricity and/or as a means to distinguish pristine vs. secondary origin of AM and FM of signals obtained by bandpass filtering and amplitude demodulation. By analogy, FM interference patterns in the precessional band can be used to interpret the phase of short eccentricity (E2 + E3). For very long records, Myr-scale modulation patterns (e.g., ~2-Myr eccentricity modulation) are a potential target for this method. Intervals that exhibit well-preserved FM of short eccentricity, but are too short for the analysis of Myr-scale FM, might still be instrumental in the assessment of long-term modulation patterns. For example, astronomical solutions indicate that the amplitude within the short-eccentricity band becomes weak and FM is indistinct during Myr-scale eccentricity nodes (Fig. S2). Continuous series of well-defined FM patterns are therefore unlikely to represent Myr-scale eccentricity minima, and can be interpreted as highs in the Myr-scale modulation. The opposite relationship (i.e., the use of indistinct FM to infer Myr-scale nodes) should not be routinely applied, because the depositional record is subject to a number of processes distorting FM.

The approach described above should be applicable to any well-preserved astronomical records. Data with a low signal-to-noise ratio will likely produce noisy FM patterns, from which it would be challenging to interpret phase with confidence. In these instances, the FM technique can be instrumental in detecting the degree of distortion and avoiding an incorrect interpretation of bandpassed signals.

4.3. Case studies from the Eocene and Cretaceous

Two exquisitely preserved eccentricity records illustrate how pristine FM patterns can be distinguished in real geological data and used to improve paleoclimate interpretation. We focus on intervals associated with major climatic and oceanographic events of the greenhouse world, whose origins remain debated.

4.3.1. Cenomanian black shales and OAE II

The Late Cenomanian to earliest Turonian OAE II was a ~700-kyr long episode of massive removal of organic carbon from the exogenic reservoir (e.g., Schlanger and Jenkyns, 1976; Arthur et al., 1988; Kuypers et al., 2004; Meyers et al., 2012a) in a world characterized by high concentrations of carbon dioxide (and likely other greenhouse gases) in the atmosphere (e.g., Berner, 2006). The increase in carbon burial due to enhanced marine productivity and anoxia (e.g., Schlanger and Jenkyns, 1976; Arthur et al., 1988; Kuypers et al., 2004) was fueled by nutrient fluxes from submarine volcanism (Snow et al., 2005; Turgeon and Creaser, 2008; Flögel et al., 2011; Du Vivier et al., 2014) superimposed upon favorable ocean circulation patterns (e.g., Trabucho Alexandre et al., 2010; Flögel et al., 2011; Zheng et al., 2013). Several studies suggest an important role for astronomically paced insolation in controlling the timing and structure of OAE II (e.g., Kuypers et al., 2004; Mitchell et al., 2008; Lanci et al., 2010; Wendler et al., 2014; Laurin et al., 2015). The culmination of OAE II has been shown to coincide with an increased obliquity variance in the low-latitude Atlantic (Meyers et al., 2012b), which was a major locus of organic carbon accumulation at that time (see review in Trabucho Alexandre et al., 2010). The timing of OAE II also fits with the rhythm of the long-term, ~1-Myr modulation of axial obliquity (e.g., Laurin et al., 2015), while some studies propose an ~2-Myr eccentricity influence (Mitchell et al., 2008; Lanci et al., 2010).

If organic matter accumulation is focused at low latitudes during OAE II (e.g., Kuypers et al., 2004; Trabucho Alexandre et al., 2010), precession and eccentricity variations are expected to play an important role via a strong control on the monsoon, and thus sedimentation (e.g., Beckmann et al., 2005). In this regard, well preserved eccentricity and precession cycles have been described from Cretaceous strata in the Mediterranean (e.g., De Boer and Wonders, 1984; Herbert and Fischer, 1986). The Furlo section located in the Umbria-Marche basin, central Italy, has received particular attention as it makes it possible to extend an exquisite eccentricity record of the Middle to Late Cenomanian to the base of the OAE II. Different studies have, however, proposed different phasings of eccentricity variations at this section, with different implications for both the regional climate forcing of anoxia in the Mediterranean and the orbital control on OAE II in general (cf. Mitchell et al., 2008; Lanci et al., 2010).

Here we reexamine published Isothermal Remanent Magnetization (IRM) data from Lanci et al. (2010). This data set provides a proxy for bottom water oxygenation of the Tethys ocean: high IRM intensities are interpreted to record detrital magnetite preservation under well-oxygenated conditions, while low IRM values are considered a product of magnetite dissolution under poorly oxygenated or euxinic bottom waters (Lanci et al., 2010). Samples were taken exclusively from limestone lithologies in order to keep the rock-magnetic record independent from lithological variations (see Lanci et al., 2010); thus the thin (cm-scale) interbedded cherts and black shales, interpreted as largely precessional in their origin (Mitchell et al., 2008), were not sampled for IRM. The effect of uneven sampling and systematic avoidance of precession-paced black shales in the IRM dataset was tested with a one-dimensional model (Fig. S1.5). The results indicate that the E2–E3 interference is resistant to this type of undersampling and provides a reliable basis for the interpretation of 405-kyr phasing.

The IRM data show well defined, statistically significant (>94 to >99% F-test significance level) spectral maxima that correspond to the eccentricity terms E1, E2 and E3, as revealed by ASM analysis (Figs. 6 and S3.2; this confirms the cycle calibration of Lanci et al., 2010). The EHA spectrogram exhibits well defined frequency patterns originating from the interference of E2 and E3 terms and meeting the criteria for pristine modulation outlined in Section 4.2 (Fig. 6c). Based on the E2–E3 interference patterns we conclude that the ~4-m minima in IRM (Fig. 6b) correspond to maxima in the 405-kyr eccentricity cycle (in this respect, our interpretation differs from that in Lanci et al., 2010, who proposed the opposite phasing).

The size of the EHA window prevents a direct evaluation of interference patterns at and immediately beneath the Bonarelli Level, which marks OAE II at Furlo. To estimate eccentricity phasing at the onset of the Bonarelli Level we integrate the 405-kyr eccentricity bandpass results from the IRM data (Fig. 6b) with the floating astrochronology of Mitchell et al. (2008); following this approach the onset of the Bonarelli Level is 390 kyr to 420 kyr younger than the last 405-kyr maximum documented with FM (Ce-3; Figs. 6b, c and S4.1). The resultant anchored astrochronology (discussed in greater detail below) is compatible with the radioisotopic constraints presented in Meyers et al. (2012a) and Eldrett et al. (2015) (Fig. S4.3). The high-resolution data of Batenburg et al. (2016) offer alternative timing options. Their tuning #1 is incompatible with radioisotopic constraints in Eldrett et al. (2015) and Meyers et al. (2012a) (see Fig. S4.3), while tuning #2 is compatible with Eldrett et al. (2015) but not Meyers et al. (2012a). Tuning #2 would place the onset of the Bonarelli Level only ~340 kyr after the Ce-3 maximum (Fig. 6b). Thus, according to the Batenburg et al. (2016) and Mitchell et al. (2008) astrochronologies, the onset of the Bonarelli Level either predates the following 405-kyr maximum (Ce-2) by 65 kyr, or coincides with this maximum

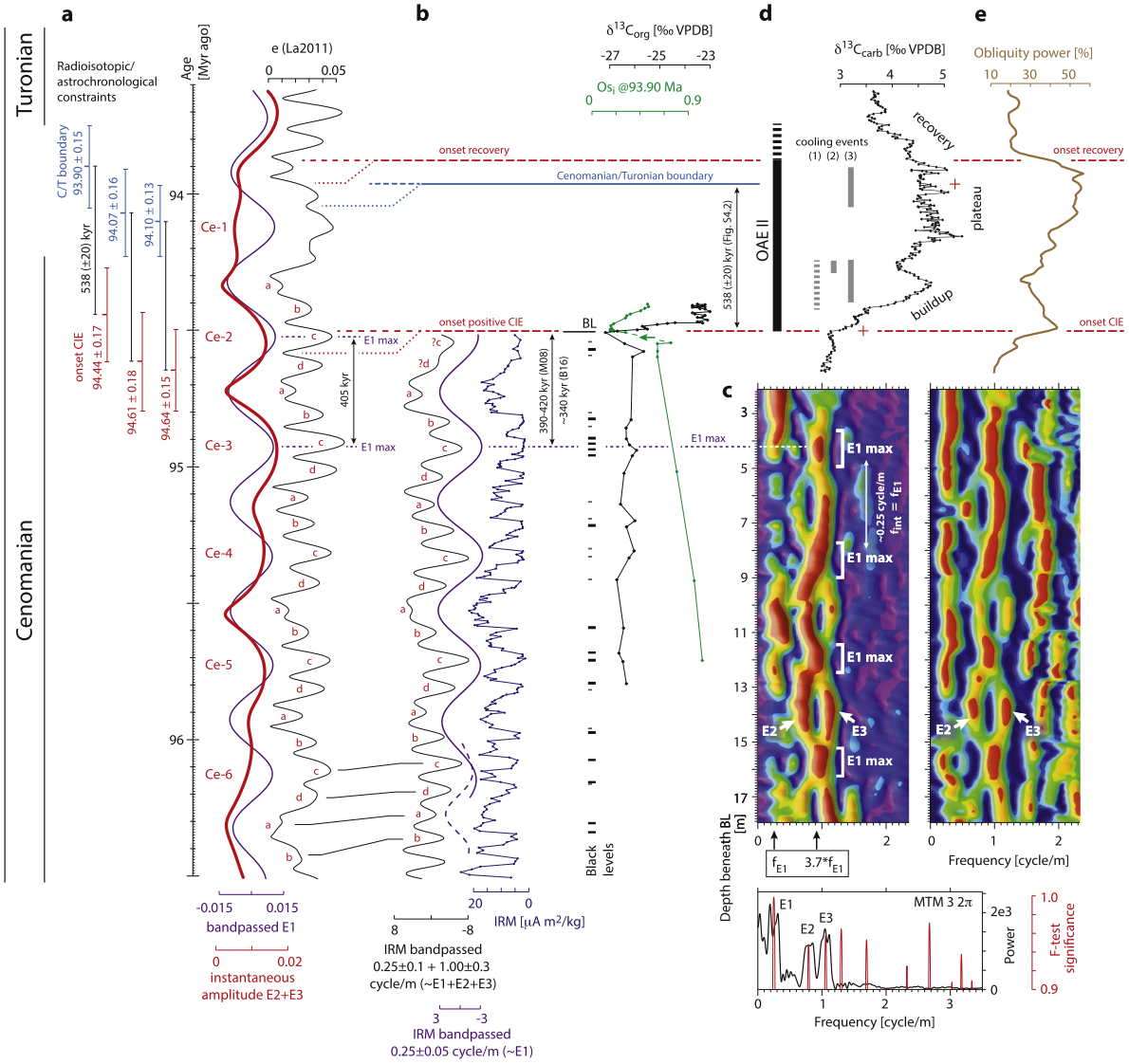

Fig. 6. Eccentricity signature in the Cenomanian at Furlo. **(a)** Geochronology and the La2011 solution (Laskar et al., 2011b): bulk eccentricity (black line), bandpassed 405-kyr term (2.5 ± 0.5 cycle/Myr, Gaussian; purple line) and instantaneous amplitude of short eccentricity (Hilbert transformed 9.5 ± 3.0 cycle/Myr, Gaussian; thick red line). Maxima in E1 (405 kyr) eccentricity are labeled Ce-1 through Ce-6 and superimposed maxima in short eccentricity are labeled a through d. Ages of the Cenomanian–Turonian boundary (C/T; 93.90 ± 0.15 Myr; Meyers et al., 2012a; 94.10 ± 0.13 or 94.07 ± 0.16 Myr; Eldrett et al., 2015), bentonite A (94.27 + 0.16/−0.17 Myr; Meyers et al., 2012a) and the onset of positive carbon-isotope excursion (CIE; estimated by adding 538 ± 20 kyr to the age of the C/T boundary; Fig. S4.2) constrain the timing of OAE II. The uncertainty in numerical timing is too large to identify the phasing of OAE II relative to the E1 phases in La2011. The relative timing of the onset of CIE vs. C/T is, however, determined with a much smaller uncertainty, ±20 kyr (Fig. S4.2). The major magmatic pulse documented in osmium isotopes (Turgeon and Creaser, 2008) predates the onset of positive CIE by ~40 kyr (phase 'ii' in Du Vivier et al., 2014; green arrow in Fig. 6b). The numerical age of 405-kyr maxima and minima in La2011 is uncertain within ±80 kyr (Fig. S4.3e); this uncertainty, however, does not affect the interpretation of 405-kyr phasing during OAE II. **(b)** Furlo section: IRM (blue line; Lanci et al., 2010), sum of bandpassed eccentricity terms (E1 + E2 + E3; 0.25 ± 0.10 + 1.00 ± 0.3 cycle/m, Gaussian; black line), bandpassed 405-kyr term (purple line: 0.25 ± 0.05 cycle/m Gaussian filter; dashed purple line: 0.30 ± 0.15 cycle/m Gaussian filter), $\delta^{13}C_{org}$ (black line; Jenkyns et al., 2007) and osmium-isotope data (green line; Du Vivier et al., 2014). Furlo section data are plotted against stratigraphic depth (scale as in Fig. 6c). Black shale and chert levels are plotted as horizontal lines to the right of the IRM data, after Lanci et al. (2010). BL = base of Bonarelli Level. The IRM curve is flipped horizontally and adjusted linearly to optimize the correlation of interpreted 405-kyr eccentricity maxima (Fig. 6c) with the eccentricity maxima in La2011 (see Fig. S4.3). It should be stressed that the interpretation of eccentricity maxima/minima is not affected by the potential instability of the La2011 solution, because the 405-kyr period is constant within 0.16% (Laskar et al., 2011a). The timing of the onset of BL relative to the latest 405-kyr maximum captured by FM patterns in EHA (Fig. 6c) is estimated using published age models: 390–420 kyr (Mitchell et al., 2008; M08; dashed correlation line), and ~340 kyr (tuning #2 of Batenburg et al., 2016; B16; dotted correlation line). **(c)** EHA amplitude (left) and F-test significance (right) spectra of IRM (MTM 3 2π; 4 m window, color scales as in Fig. 7). MTM power spectrum and F-test significance for the entire interval are shown at the bottom. Junctions in the E2 + E3 trace occur systematically, in the same rhythm as the E1 signal and are therefore interpreted as 405-kyr maxima (E1 max). **(d)** $\delta^{13}C_{carb}$ signature of OAE II, Eastbourne section (Paul et al., 1999), calibrated in the time domain (Fig. S4.2; red crosses indicate age control points). The timing of cooling events in Europe and proto-Atlantic: 1 = TEX_{86} cooling in the North Atlantic (Forster et al., 2007; Sinninghe Damsté et al., 2010; van Helmond et al., 2014), 2 = plenus cool fauna in Europe (Voigt et al., 2006), 3 = $\delta^{18}O_{carb}$, Eastbourne (Gambacorta et al., 2015). **(e)** Changes in the power attributed to axial obliquity (Site 1261B, tropical Atlantic) calibrated in the time domain and anchored at the base of the positive CIE (Meyers et al., 2012b). (For interpretation of the references to color in this figure legend, the reader is referred to the web version of this article.)

within ±15 kyr (Fig. 6). These estimates further imply that the onset of the osmium-isotope excursion (Turgeon and Creaser, 2008; Du Vivier et al., 2014; Fig. 6b), lithium-isotope excursion (Pogge von Strandmann et al., 2013) and 'precursor events' documented locally (Eldrett et al., 2015) are either coeval with or predate the 405-kyr maximum. Of prime importance for understanding the internal dynamics of OAE II is the onset and acceleration of the positive carbon-isotope ($\delta^{13}C$) excursion, which should be linked to the rate of global carbon burial (e.g., Arthur et al., 1988). The excursion starts immediately above the base of the Bonarelli Level

(Jenkyns et al., 2007; Gambacorta et al., 2015); its onset is therefore considered contemporaneous with the Ce-2 eccentricity maximum within the −65/+15 kyr uncertainty inferred above.

Just above the analyzed interval at Furlo, the OAE II is highly condensed; however the details of the event can be examined at other localities. Here we use the high-resolution $\delta^{13}C_{carb}$ record from the Eastbourne section (Paul et al., 1999) and calibrate these data in the time domain based on published astronomical and radioisotopic time scales for this interval (Sageman et al., 2006; Meyers et al., 2012a; Ma et al., 2014; Eldrett et al., 2015; see Fig. S4.2). Floating astrochronologies for the Portland and Angus cores (Sageman et al., 2006; Ma et al., 2014) are correlated to the Eastbourne section using carbon-isotope stratigraphy and biostratigraphy (Fig. S4.2). The Eastbourne $\delta^{13}C_{carb}$ curve is then aligned with the Furlo record along the base of the positive carbon-isotope excursion (Jenkyns et al., 2007; Gambacorta et al., 2015; Fig. 6). This correlation is further supported by osmium-isotope data from Furlo and Portland (Du Vivier et al., 2014).

Although the uncertainty in numerical dating of the onset and termination of OAE II are on the order of ±150 kyr (Meyers et al., 2012a; Eldrett et al., 2015), the uncertainty of the floating time scale duration is an order of magnitude smaller (Fig. 6) and thus makes it possible to evaluate the timing of OAE II relative to the 405-kyr eccentricity cycle (whose period is stable within 0.16%; Laskar et al., 2011a). The integration of phase-calibrated Furlo IRM data with age-calibrated Eastbourne $\delta^{13}C_{carb}$ data suggests that the major buildup phase of OAE II (defined by the highest gradient in rising $\delta^{13}C$; first buildup in Paul et al., 1999) was coincident with the maximum through declining phases of the 405-kyr eccentricity cycle Ce-2 (and maximum through declining amplitudes of the total E1 + E2 + E3 eccentricity; Fig. 6). Drawdown in pCO_2 due to carbon sequestration (e.g., Barclay et al., 2010) and transient cooling in the Atlantic and Europe (Voigt et al., 2006; Forster et al., 2007; Sinninghe Damsté et al., 2010; Zheng et al., 2013; van Helmond et al., 2014; Gambacorta et al., 2015) occurred during the phase of declining and low eccentricity amplitudes following the Ce-2 maximum (Fig. 6; note that another cooling phase, interpreted by Gambacorta et al., 2015, possibly overlaps with the following 405-kyr minimum). The plateau phase of OAE II (Paul et al., 1999) coincides with a 405-kyr eccentricity maximum, which according to the latest orbital solution La2011 (Laskar et al., 2011b) represents a minimum in the very long term (~2.2 Myr) cycle of short-eccentricity AM (red line in Fig. 6a). The recovery phase documented by the onset of declining $\delta^{13}C$ values c. 80 kyr after the Cenomanian–Turonian boundary starts within ±70 kyr of a 405-kyr minimum and continues during a resumed rise in the short-eccentricity amplitudes and runup towards another 405-kyr maximum (Fig. 6).

Although the Myr-scale modulation in La2011 involves a degree of uncertainty beyond ~50 Myr ago (Westerhold et al., 2012), the possibility of OAE II being centered at a ~2.2-Myr node in eccentricity amplitudes (Fig. 6a) can be evaluated using the FM preservation at Furlo. A comparison of inherent variability in FM (Fig. S2) with the series of 3 to 4 well-defined cycles of 405-kyr modulation beneath OAE II (Fig. 6c) suggests that the interval 0.3 Myr to 1.7 Myr prior to the onset of OAE II is unlikely to accommodate a Myr-scale node. Thus, if the Cenomanian modulation maintains a 2.2–2.4 Myr rhythm as in most of the Cenozoic, then one of the nodes must overlap with the event.

The FM signature at Furlo suggests that approximately two-thirds of the black shales and cherts underlying the Bonarelli Level (Fig. 6b) formed at or near maxima in 405-kyr eccentricity. By analogy, most of the shorter-term bundles (and sometimes individual layers) correspond to maxima in the ~100-kyr (E2 + E3) eccentricity (Fig. 6a, b), in agreement with the hypothesis of monsoonal forcing of anoxia prior to OAE II in this area (cf. Mitchell et al., 2008). Importantly, black shales and cherts are absent from 405-kyr minima at this section. Considering the overlap of OAE II with one or two 405-kyr minima, the anoxic conditions of OAE II (represented by the Bonarelli Level at Furlo) stand out as a qualitatively distinct response to external forcing, and cannot be considered a mere intensification of the background (monsoonal) variability.

The coincidence of the buildup and recovery of OAE II with opposite phases of the 405-kyr eccentricity cycle and the inferred overlap of OAE II with a ~2.2 Myr eccentricity minimum, do not constitute direct evidence for a causal relationship between OAE II and astronomical forcing. Given the role of eccentricity in the global carbon cycle (e.g., Lourens et al., 2005; Pälike et al., 2006; Zachos et al., 2010; Valero et al., 2014), however, it is reasonable to consider a contribution of eccentricity phasing to the internal dynamics of the event. Low eccentricity implies moderate seasonality lacking both extremely low and extremely high seasonal contrasts at the precessional scale. Because the contribution of precessional index (and thus eccentricity) to insolation series is greatest at low latitudes, the reduced eccentricity provides suitable grounds for both the enhanced obliquity influence during OAE II (Meyers et al., 2012b; Fig. 6e) and increase in the role of higher latitude processes in ocean circulation and the carbon cycle (e.g., Meyers et al., 2012b; Zheng et al., 2013; Laurin et al., 2015). We hypothesize that the shift of intermediate/deep water source towards higher latitudes and its influence on carbon sequestration during OAE II (Meyers et al., 2012b) could be facilitated by subdued short-eccentricity amplitudes during a Myr-scale eccentricity minimum.

A causal role of eccentricity phasing could help to explain the delayed onset of OAE II relative to the initiation of volcanic activity (Turgeon and Creaser, 2008; Du Vivier et al., 2014), and the timing of transient cooling episodes (Voigt et al., 2006; Forster et al., 2007; Sinninghe Damsté et al., 2010; Zheng et al., 2013; van Helmond et al., 2014; Gambacorta et al., 2015). Uncertainties in the timing and phasing of the individual segments of OAE II, however, persist, preventing a detailed evaluation of these potential relationships. It is also stressed that OAE II cannot be fully understood without additional controls such as enhanced volcanic nutrient fluxes (Snow et al., 2005; Turgeon and Creaser, 2008), changing weathering rates (Pogge von Strandmann et al., 2013), particular ocean-circulation patterns (e.g., Trabucho Alexandre et al., 2010; Flögel et al., 2011) and favorable configuration of the long-term obliquity cycle (e.g., Meyers et al., 2012b; Wendler et al., 2014; Laurin et al., 2015).

4.3.2. Eocene hyperthermals

The Early Eocene interval is marked by a series of brief climate perturbations characterized by warming of sea-surface temperatures, lysocline shallowing and negative carbon-isotope anomalies (e.g., Zachos et al., 2010). Following the Paleocene–Eocene Thermal Maximum (PETM) the most prominent of these events, or hyperthermals, were the ETM2 ('Elmo') and ETM3 ('X'), accompanied by smaller scale events such as H2 and I1 (e.g., Zachos et al., 2010; Fig. 7). The link of hyperthermals to high eccentricity has been proposed in previous studies based on the elapsed time observed between events, and the AM of preserved short-eccentricity cycles (Lourens et al., 2005; Westerhold et al., 2007; Galeotti et al., 2010). The possibility of low-eccentricity forcing of hyperthermals was pointed out recently (Smith et al., 2014, their Scenario 1). An independent test of the 405-kyr eccentricity phasing of the hyperthermals is conducted here through evaluation of FM.

Carbonate-content data from the Contessa section, Umbria-Marche basin (Galeotti et al., 2010) show statistically significant power-spectral maxima (>98% F-test confidence level) correspond-

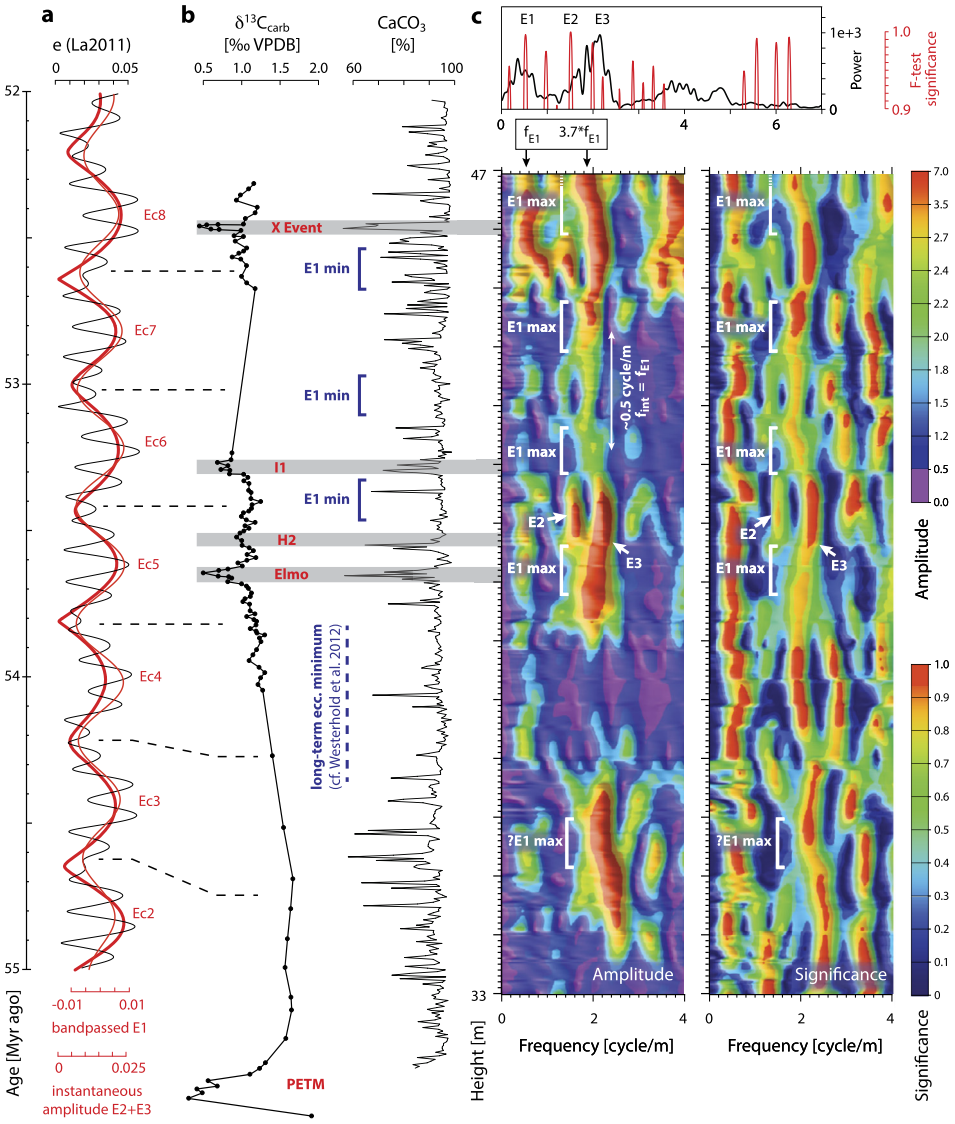

Fig. 7. Eccentricity signature in the Lower Eocene, Contessa. **(a)** Total eccentricity (black), bandpassed 405-kyr term ($2.5 + -0.5$ cycle/Myr, Gaussian; thin red) and instantaneous amplitude of short eccentricity (Hilbert transformed 9.5 ± 2.5 cycle/Myr, Gaussian; thick red) in the solution La2011 (Laskar et al., 2011b). Maxima in 405-kyr eccentricity are labeled Ec2 through Ec8 following Westerhold et al. (2012). **(b)** $\delta^{13}C_{carb}$ signatures of Eocene hyperthermals (gray bands), and high-resolution $CaCO_3$ data, Contessa Road section (Galeotti et al., 2010). **(c)** Time-series analysis of the $CaCO_3$ data: MTM power spectrum and F-test significance for the whole interval (MTM 3 2π; top); EHA amplitude and probability spectra (MTM 3 2π; 5 m window; bottom). The trace of the E2 + E3 signal exhibits systematic alternations of intervals of positive and negative interference, in the upper part of the section. These junctions and bifurcations exhibit the same rhythm as the E1 signal and are therefore interpreted as maxima and minima, respectively, of the 405-kyr eccentricity cycle (cf. Figs. 1, 3, 4, and S1). The E2 + E3 signal is poorly distinguishable in the interval 36.5–39 m, coincident with a minimum in the very long-term cycle of eccentricity modulation in La2011 (thick red line in Fig. 7a; cf. Westerhold et al., 2012). The interval is linearly adjusted so that E1 maxima in La2011 are aligned with the interpreted E1 maxima (E1 max). This tuning suggests that the major hyperthermals (except the PETM, which can not be evaluated here) occur at or near the maxima in 405-kyr eccentricity. (For interpretation of the references to color in this figure legend, the reader is referred to the web version of this article.)

ing to the E1, E2 and E3 terms, as calibrated by ASM analysis (Figs. 7c and S5; this confirms the cycle calibration of Galeotti et al., 2010). In the upper half of the section, spatial expression of the E2 and E3 cycles suggests systematic interferences associated with E1. By analogy with the above stratigraphic models (Section 4.2), the intervals of positive interference are interpreted as maxima in the 405-kyr eccentricity cycle. These patterns suggest that the AM studied by Galeotti et al. (2010) is indeed close to the primary modulation of the eccentricity signal. The hyperthermals ETM2 ('Elmo'), I1 and ETM3 ('X') overlap with broad intervals of positive interference in the E2–E3 band. The event H2 is offset towards a phase of negative interference, but none of these hyperthermals overlaps with a minimum in the 405-kyr eccentricity (E1min in Fig. 7). It can be concluded that all events (except the PETM, which can not be evaluated here) occur within 100 kyr (±90 degrees) of 405-kyr maxima, which is in agreement with the hypotheses invoking a causal role for pronounced seasonal extremes in the forcing mechanism (cf. Lourens et al., 2005; Lunt et al., 2011; Galeotti et al., 2010; Zachos et al., 2010).

5. Conclusions

Interference patterns accompanying FM in the short-eccentricity band (~95 and 124 kyr) provide a robust basis for distinguishing pristine AM and FM from depositional artifacts, and thus make it possible to interpret the phase of astronomical forcing. Pristine FM is marked by a systematic interference of the ~95-kyr and ~124-kyr terms that occur with a 405-kyr rhythm; even if the stratigraphic record lacks a distinct 405-kyr cycle, the interference

patterns should follow the periodicity $p_{\text{int}} = [(p_{i2} + p_{i3})/2] * (3.7 \pm 0.2)$, where p_{i2} and p_{i3} are the spatial periods, i.e., reciprocals of spatial frequencies, of the interfering components (i.e., ~124 and ~95 kyr eccentricity; cf. Rial, 1999). Distortions in the modulation related to climate/depositional system response and sampling lack this rhythm and/or exhibit a 'red' or 'blue shift' of the interfering frequencies, providing a diagnostic to identify such records as unsuitable for phase assessment. We propose that AM and FM patterns obtained through bandpass filtering and demodulation should be routinely validated using the above criteria, specifically if the phasing of the signal is of interest. This approach is applicable to evaluate any frequency-modulated signal that expresses bifurcations (short eccentricity and precession).

Detection of the 405-kyr eccentricity phasing based on FM helps to constrain the astronomical control on paleoclimate change in intervals lacking a stable astronomical solution and/or high-resolution numerical dating. As an example, the results presented here provide independent support for a high-eccentricity forcing of the Early Eocene hyperthermals ETM2 ('Elmo'), ETM3 ('X'), H2 and I1, suggesting a leading role for pronounced seasonal extremes in destabilizing terrestrial or marine carbon reservoirs (e.g., Lunt et al., 2011; Zachos et al., 2010) or triggering ventilation of a dissolved organic carbon pool (Sexton et al., 2011). In contrast to the greenhouse gas emission events associated with Eocene hyperthermals, the same (maximum) eccentricity phase promoted carbon burial in the Mediterranean region during the Middle and Late Cenomanian, prior to the global anoxic event OAE II. A comparison of different regional and global responses to a single orbital configuration superimposed upon a secular transition from the Cretaceous greenhouse towards icehouse should facilitate our understanding of the evolving oceanographic responses to astronomical forcing.

The eccentricity phasing of the late-Cretaceous OAE II is also evaluated. The buildup of the positive carbon-isotope excursion coincides with a maximum and subsequent fall in 405-kyr eccentricity, while the recovery correlates with the opposite (i.e., minimum and rising) phases of the 405-kyr cycle. The body of the event is associated with very weak short eccentricity cycles during a 2.2 Myr eccentricity node, according to the solution La2011 (Laskar et al., 2011b) and in agreement with observed FM. This configuration provides a context for the transient cooling, propagation of a high-latitude signal towards the equator and enhanced obliquity variance in this interval, as documented in previous studies (Meyers et al., 2012b). We infer that reduced eccentricity amplitudes and corresponding low seasonality variation played a vital role in the mechanism controlling high productivity, anoxia and efficient carbon sequestration during OAE II.

Acknowledgements

This research was supported by the Ministry of Education, Youth and Sports, Czech Republic (grant LH12041). JL acknowledges support by research program RVO67985530 of the Academy of Sciences of the Czech Republic. SRM acknowledges support from U.S. National Science Foundation award EAR-1151438. J. Laskar kindly provided the La2011 eccentricity solution. We are grateful for the constructive reviews from Sietske Batenburg and an anonymous reviewer, which improved the manuscript.

Appendix A. Supplementary material

Supplementary material related to this article can be found online at http://dx.doi.org/10.1016/j.epsl.2016.02.047.

References

Arthur, M.A., Dean, W.E., Pratt, L.M., 1988. Geochemical and climatic effects of increased marine organic carbon burial at the Cenomanian/Turonian boundary. Nature 335, 714–717. http://dx.doi.org/10.1038/335714a0.

Barclay, R.S., McElwain, J.C., Sageman, B.B., 2010. Carbon sequestration activated by a volcanic CO_2 pulse during Ocean Anoxic Event 2. Nat. Geosci. 3, 205–208. http://dx.doi.org/10.1038/ngeo757.

Batenburg, S.J., De Vleeschouwer, D., Sprovieri, M., Hilgen, F.J., Gale, A.S., Singer, B.S., Koeberl, C., Coccioni, R., Claeys, P., Montanari, A., 2016. Orbital control on the timing of oceanic anoxia in the Late Cretaceous. Clim. Past Discuss. http://dx.doi.org/10.5194/cp-2015-182.

Beckmann, B., Flögel, S., Hofmann, P., Schulz, M., Wagner, T., 2005. Orbital forcing of Cretaceous river discharge in tropical Africa and ocean response. Nature 437, 241–244. http://dx.doi.org/10.1038/nature03976.

Berger, A., Loutre, M.-F., Tricot, C., 1993. Insolation and Earth's orbital periods. J. Geophys. Res. 98 (D6), 10341–10362. http://dx.doi.org/10.1029/93JD00222.

Berner, R.A., 2006. GEOCARBSULF: a combined model for Phanerozoic atmospheric O_2 and CO_2. Geochim. Cosmochim. Acta 70, 5653–5664. http://dx.doi.org/10.1016/j.gca.2005.11.032.

Boylan, A.L., Waltham, D.A., Bosence, D.W.J., Badenas, B., Aurell, M., 2002. Digital rocks: linking forward modelling to carbonate facies. Basin Res. 14, 401–415. http://dx.doi.org/10.1046/j.1365-2117.2002.00180.x.

De Boer, P.L., Wonders, A.A.H., 1984. Astronomically induced rhythmic bedding in Cretaceous pelagic sediments near Moria (Italy). In: Berger, A., Imbrie, J., Hays, J., Kukla, G., Saltzman, B. (Eds.), Milankovitch and Climate, Part 1. D. Reidel Publishing Company, Boston, MA, pp. 177–190.

Du Vivier, A.D.C., Selby, D., Sageman, B.B., Jarvis, I., Gröcke, D.R., Voigt, S., 2014. Marine $^{187}Os/^{188}Os$ isotope stratigraphy reveals the interaction of volcanism and ocean circulation during Oceanic Anoxic Event 2. Earth Planet. Sci. Lett. 389, 23–33. http://dx.doi.org/10.1016/j.epsl.2013.12.024.

Eldrett, J.S., Ma, C., Bergman, S.C., Lutz, B., Gregory, F.J., Dodsworth, P., Phipps, M., Hardas, P., Minisini, D., Ozkan, A., Ramezani, J., Bowring, S.A., Kamo, S.L., Ferguson, K., Macaulay, C., Kelly, A.E., 2015. An astronomically calibrated stratigraphy of the Cenomanian, Turonian and earliest Coniacian from the Cretaceous Western Interior Seaway, USA: implications for global chronostratigraphy. Cretac. Res. 56, 316–344. http://dx.doi.org/10.1016/j.cretres.2015.04.010.

Flögel, S., Wallmann, K., Poulsen, C.J., Zhou, J., Oschlies, A., Voigt, S., Kuhnt, W., 2011. Simulating the biogeochemical effects of volcanic CO_2 degassing on the oxygen-state of the deep ocean during the Cenomanian/Turonian Anoxic Event (OAE2). Earth Planet. Sci. Lett. 305, 371–384. http://dx.doi.org/10.1016/j.epsl.2011.03.018.

Forster, A., Schouten, S., Moriya, K., Wilson, P.A., Sinninghe Damsté, J.S., 2007. Tropical warming and intermittent cooling during the Cenomanian/Turonian oceanic anoxic event 2: sea surface temperature records from the equatorial Atlantic. Paleoceanography 22, PA1219. http://dx.doi.org/10.1029/2006PA001349.

Galeotti, S., Krishnan, S., Pagani, M., Lanci, L., Gaudio, A., Zachos, J.C., Monechi, S., Morelli, G., Lourens, L., 2010. Orbital chronology of Early Eocene hyperthermals from the Contessa Road section, central Italy. Earth Planet. Sci. Lett. 290, 192–200. http://dx.doi.org/10.1016/j.epsl.2009.12.021.

Gambacorta, G., Jenkyns, H.C., Russo, F., Tsikos, H., Wilson, P.A., Faucher, G., Erba, E., 2015. Carbon- and oxygen-isotope records of mid-Cretaceous Tethyan pelagic sequences from the Umbria–Marche and Belluno Basins (Italy). Newsl. Stratigr. 48, 299–323. http://dx.doi.org/10.1127/nos/2015/0066.

Hays, J.D., Imbrie, J., Shackleton, N.J., 1976. Variations in the Earth's Orbit: pacemaker of the Ice Ages. Science 194, 1121–1132. http://dx.doi.org/10.1126/science.194.4270.1121.

Herbert, T.D., 1992. Paleomagnetic calibration of Milankovitch cyclicity in Lower Cretaceous sediments. Earth Planet. Sci. Lett. 112, 15–28.

Herbert, T.D., 1997. A long marine history of carbon cycle modulation by orbital-climatic changes. Proc. Natl. Acad. Sci. 94, 8362–8369.

Herbert, T.D., Fischer, A.G., 1986. Milankovitch climatic origin of the mid-Cretaceous black shale rhythms in central Italy. Nature 321, 739–743.

Herbert, T.D., Gee, J., DiDonna, S., 1999. Precessional cycles in Upper Cretaceous pelagic sediments of the South Atlantic: long-term patterns from high-frequency climate variations. In: Barrera, E., Johnson, C.C. (Eds.), Evolution of the Cretaceous Ocean-Climate System. In: Spec. Pap., Geol. Soc. Am., vol. 332, pp. 105–120.

Hilgen, F.J., 1991. Astronomical calibration of Gauss to Matuyama sapropels in the Mediterranean and implication for the geomagnetic polarity time scale. Earth Planet. Sci. Lett. 104, 226–244. http://dx.doi.org/10.1016/0012-821X(91)90206-W.

Hinnov, L.A., 2000. New perspectives on orbitally forced stratigraphy. Annu. Rev. Earth Planet. Sci. 28, 419–475. http://dx.doi.org/10.1146/annurev.earth.28.1.419.

Hinnov, L.A., Park, J.J., 1998. Detection of astronomical cycles in the stratigraphic record by frequency modulation (FM) analysis. J. Sediment. Res. 68, 524–539.

Huybers, P., Aharonson, O., 2010. Orbital tuning, eccentricity, and the frequency modulation of climatic precession. Paleoceanography 25, PA4228.

Imbrie, J., Berger, A., Boyle, E.A., Clemens, S.C., Duffy, A., Howard, W.R., Kukla, G., Kutzbach, J., Martinson, D.G., McIntyre, A., Mix, A.C., Molfino, B., Morley, J.J., Peterson, L.C., Pisias, N.G., Prell, W.L., Raymo, M.E., Shackleton, N.J., Toggweiler, J.R., 1993. On the structure and origin of major glaciation cycles: 2. The 100,000-year cycle. Paleoceanography 8, 699–735. http://dx.doi.org/10.1029/93PA02751.

Jenkyns, H.C., Matthews, A., Tsikos, H., Erel, Y., 2007. Nitrate reduction, sulfate reduction, and sedimentary iron isotope evolution during the Cenomanian–Turonian oceanic anoxic event. Paleoceanography 22, PA3208. http://dx.doi.org/10.1029/2006PA001355.

Kuypers, M.M.M., Lourens, L.J., Rijpstra, W.I.C., Pancost, R.D., Nijenhuis, I.A., Sinninghe Damsté, J.S., 2004. Orbital forcing of organic carbon burial in the proto-North Atlantic during oceanic anoxic event 2. Earth Planet. Sci. Lett. 228, 465–482. http://dx.doi.org/10.1016/j.epsl.2004.09.037.

Lanci, L., Muttoni, G., Erba, E., 2010. Astronomical tuning of the Cenomanian Scaglia Bianca Formation at Furlo, Italy. Earth Planet. Sci. Lett. 292, 231–237. http://dx.doi.org/10.1016/j.epsl.2010.01.041.

Laskar, J., Joutel, F., Boudin, F., 1993. Orbital, precessional, and insolation quantities for the Earth from −20 Myr to +10 Myr. Astron. Astrophys. 270, 522–533.

Laskar, J., Robutel, P., Joutel, F., Gastineau, M., Correia, A.C.M., Levrard, B., 2004. A long-term numerical solution for the insolation quantities of the Earth. Astron. Astrophys. 428, 261–285. http://dx.doi.org/10.1051/0004-6361:20041335.

Laskar, J., Fienga, A., Gastineau, M., Manche, H., 2011a. La2010: a new orbital solution for the long term motion of the Earth. Astron. Astrophys. 532, A89. http://dx.doi.org/10.1051/0004-6361/201116836.

Laskar, J., Gastineau, M., Delisle, J.-B., Farrés, A., Fienga, A., 2011b. Strong chaos induced by close encounters with Ceres and Vesta. Astron. Astrophys. 532, L4. http://dx.doi.org/10.1051/0004-6361/201117504.

Laurin, J., Čech, S., Uličný, D., Štaffen, Z., Svobodová, M., 2014. Astrochronology of the Late Turonian: implications for the behavior of the carbon cycle at the demise of peak greenhouse. Earth Planet. Sci. Lett. 394, 254–269. http://dx.doi.org/10.1016/j.epsl.2014.03.023.

Laurin, J., Meyers, S.R., Sageman, B.B., Waltham, D., 2005. Phase-lagged amplitude modulation of hemipelagic cycles: a potential tool for recognition and analysis of sea-level change. Geology 33 (7), 569–572. http://dx.doi.org/10.1130/G21350.1.

Laurin, J., Meyers, S.R., Uličný, D., Jarvis, I., Sageman, B.B., 2015. Axial obliquity control on the greenhouse carbon budget through middle- to high-latitude reservoirs. Paleoceanography 30 (2), 133–149. http://dx.doi.org/10.1002/2014PA002736.

Lourens, L.J., Sluijs, A., Kroon, D., Zachos, J.C., Thomas, E., Röhl, U., Bowles, J., Raffi, I., 2005. Astronomical pacing of late Palaeocene to early Eocene global warming events. Nature 435, 1083–1087. http://dx.doi.org/10.1038/nature03814.

Lunt, D.J., Ridgwell, A., Sluijs, A., Zachos, J., Hunter, S., Haywood, A., 2011. A model for orbital pacing of methane hydrate destabilization during the Palaeogene. Nat. Geosci. 4, 775–778. http://dx.doi.org/10.1038/ngeo1266.

Ma, C., Meyers, S.R., Sageman, B.B., Singer, B.S., Jicha, B.R., 2014. Testing the astronomical time scale for oceanic anoxic event 2, and its extension into Cenomanian strata of the Western Interior Basin (USA). Geol. Soc. Am. Bull. 126, 974–989.

Meyers, S.R., 2014. Astrochron: an R Package for Astrochronology (Version 0.3.1), http://www.geology.wisc.edu/~smeyers.

Meyers, S.R., 2015. The evaluation of eccentricity-related amplitude modulation and bundling in paleoclimate data: an inverse approach for astrochronologic testing and time scale optimization. Paleoceanography 30. http://dx.doi.org/10.1002/2015PA002850.

Meyers, S.R., Sageman, B.B., 2004. Detection, quantification, and significance of hiatuses in pelagic and hemipelagic strata. Earth Planet. Sci. Lett. 224, 55–72. http://dx.doi.org/10.1016/j.epsl.2004.05.003.

Meyers, S.R., Sageman, B.B., 2007. Quantification of deep-time orbital forcing by average spectral misfit. Am. J. Sci. 307, 773–792. http://dx.doi.org/10.2475/05.2007.01.

Meyers, S.R., Sageman, B.B., Hinnov, L.A., 2001. Integrated quantitative stratigraphy of the Cenomanian–Turonian Bridge Creek Limestone Member using evolutive harmonic analysis and stratigraphic modeling. J. Sediment. Res. 71, 628–644.

Meyers, S.R., Sageman, B.B., Pagani, M., 2008. Resolving Milankovitch: consideration of signal and noise. Am. J. Sci. 308, 770–786. http://dx.doi.org/10.2475/06.2008.02.

Meyers, S.R., Siewert, S.E., Singer, B.S., Sageman, B.B., Condon, D.J., Obradovich, J.D., Jicha, B.R., Sawyer, D.A., 2012a. Intercalibration of radioisotopic and astrochronologic time scales for the Cenomanian–Turonian boundary interval, Western Interior Basin, USA. Geology 40, 7–10. http://dx.doi.org/10.1130/G32261.1.

Meyers, S.R., Sageman, B.B., Arthur, M.A., 2012b. Obliquity forcing of organic matter accumulation during Oceanic Anoxic Event 2. Paleoceanography 27, PA3212. http://dx.doi.org/10.1029/2012PA002286.

Mitchell, R.N., Bice, D.M., Montanari, A., Cleaveland, L.C., Christianson, K.T., Coccioni, R., Hinnov, L.A., 2008. Oceanic anoxic cycles? Orbital prelude to the Bonarelli Level (OAE 2). Earth Planet. Sci. Lett. 26, 1–16. http://dx.doi.org/10.1016/j.epsl.2007.11.026.

Pälike, H., Norris, R.D., Herrle, J.O., Wilson, P.A., Coxall, H.K., Lear, C.H., Shackleton, N.J., Tripati, A.K., Wade, B.S., 2006. The heartbeat of the Oligocene climate system. Science 314, 1894–1898.

Paul, C.R.C., Lamolda, M.A., Mitchell, S.F., Vaziri, M.R., Gorostidi, A., Marshall, J.D., 1999. The Cenomanian–Turonian boundary at Eastbourne (Sussex, UK): a proposed European reference section. Palaeogeogr. Palaeoclimatol. Palaeoecol. 150, 83–121. http://dx.doi.org/10.1016/S0031-0182(99)00009-7.

Pogge von Strandmann, P.A.E., Jenkyns, H.C., Woodfine, R.G., 2013. Lithium isotope evidence for enhanced weathering during Oceanic Anoxic Event 2. Nat. Geosci. 6, 668–672. http://dx.doi.org/10.1038/NGEO1875.

R Core Team, 2015. R: a language and environment for statistical computing. R Foundation for Statistical Computing, Vienna, Austria. http://www.R-project.org/.

Rial, J.A., 1999. Pacemaking the ice ages by frequency modulation of Earth's orbital eccentricity. Science 285, 564–568.

Ripepe, M., Fischer, A.G., 1991. Stratigraphic rhythms synthesized from orbital variations. In: Franseen, K., Watney, W.L., Kendall, C.G.St.C., Ross, W. (Eds.), Sedimentary Modeling: Computer Simulations and Methods for Improved Parameter Definition. In: Kansas State Geol. Surv. Bull., vol. 233, pp. 335–344.

Ruddiman, W.F., 2006. What is the timing of orbital-scale monsoon changes? Quat. Sci. Rev. 25, 657–658. http://dx.doi.org/10.1016/j.quascirev.2006.02.004.

Sageman, B.B., Meyers, S.R., Arthur, M.A., 2006. Orbital time scale and new C-isotope record for Cenomanian–Turonian boundary stratotype. Geology 34, 125.

Schlanger, S., Jenkyns, H., 1976. Cretaceous oceanic anoxic events: causes and consequences. Geol. Mijnb. 55, 179–184.

Sexton, P.F., Norris, R.D., Wilson, P.A., Pälike, H., Westerhold, T., Röhl, U., Bolton, C.T., Gibbs, S., 2011. Eocene global warming events driven by ventilation of oceanic dissolved organic carbon. Nature 471, 349–352. http://dx.doi.org/10.1038/nature09826.

Shackleton, N.J., Hagelberg, T.K., Crowhurst, S.J., 1995. Evaluating the success of astronomical tuning: pitfalls of using coherence as a criterion for assessing pre-Pleistocene timescales. Paleoceanography 10 (4), 693–697. http://dx.doi.org/10.1029/95PA01454.

Sinninghe Damsté, J.S., van Bentum, E.C., Reichart, G.-J., Pross, J., Schouten, S., 2010. A CO_2 decrease-driven cooling and increased latitudinal temperature gradient during the mid-Cretaceous Oceanic Anoxic Event 2. Earth Planet. Sci. Lett. 293, 97–103. http://dx.doi.org/10.1016/j.epsl.2010.02.027.

Smith, M.E., Carroll, A.R., Scott, J.J., Singer, B.S., 2014. Early Eocene carbon isotope excursions and landscape destabilization at eccentricity minima: Green River Formation of Wyoming. Earth Planet. Sci. Lett. 403, 393–406. http://dx.doi.org/10.1016/j.epsl.2014.06.024.

Snow, L.J., Duncan, R.A., Bralower, T.J., 2005. Trace element abundances in the Rock Canyon Anticline, Pueblo, Colorado, marine sedimentary section and their relationship to Caribbean plateau construction and oxygen anoxic event 2. Paleoceanography 20, PA3005. http://dx.doi.org/10.1029/2004PA001093.

Thomson, D.J., 1982. Spectrum estimation and harmonic analysis. Proc. IEEE 70, 1055–1096. http://dx.doi.org/10.1109/PROC.1982.12433.

Trabucho Alexandre, J., Tuenter, E., Henstra, G.A., van der Zwan, K.J., van de Wal, R.S.W., Dijkstra, H.A., de Boer, P.L., 2010. The mid-Cretaceous North Atlantic nutrient trap: black shales and OAEs. Paleoceanography 25, PA4201. http://dx.doi.org/10.1029/2010PA001925.

Turgeon, S.C., Creaser, R.A., 2008. Cretaceous oceanic anoxic event 2 triggered by a massive magmatic episode. Nature 454, 323–326. http://dx.doi.org/10.1038/nature07076.

Valero, L., Garcés, M., Cabrera, L., Costa, E., Sáez, A., 2014. 20 Myr of eccentricity paced lacustrine cycles in the Cenozoic Ebro Basin. Earth Planet. Sci. Lett. 408, 183–193. http://dx.doi.org/10.1016/j.epsl.2014.10.007.

van Helmond, N.A.G.M., Sluijs, A., Reichart, G.-J., Sinninghe Damsté, J.S., Slomp, C.P., Brinkhuis, H., 2014. A perturbed hydrological cycle during Oceanic Anoxic Event 2. Geology 42, 123–126. http://dx.doi.org/10.1130/G34929.1.

Voigt, S., Gale, A.S., Voigt, T., 2006. Sea-level change, carbon cycling and palaeoclimate during the Late Cenomanian of northwest Europe, an integrated palaeoenvironmental analysis. Cretac. Res. 27, 836–858. http://dx.doi.org/10.1016/j.cretres.2006.04.005.

Waltham, D., 2015. Milankovitch period uncertainties and their impact on cyclostratigraphy. J. Sediment. Res. 85, 990–998. http://dx.doi.org/10.2110/jsr.2015.66.

Wendler, J.E., Meyers, S.R., Wendler, I., Kuss, J., 2014. A million-year-scale astronomical control on Late Cretaceous sea-level. Newsl. Stratigr. 47, 1–19. http://dx.doi.org/10.1127/0078-0421/2014/0038.

Westerhold, T., Röhl, U., Laskar, J., Raffi, I., Bowles, J., Lourens, L.J., Zachos, J.C., 2007. On the duration of magnetochrons C24r and C25n and the timing of early Eocene global warming events: implications from the Ocean Drilling Program Leg 208 Walvis Ridge depth transect. Paleoceanography 22, PA2201.

Westerhold, T., Röhl, U., Laskar, J., 2012. Time scale controversy: accurate orbital calibration of the early Paleogene. Geochem. Geophys. Geosyst. 13, Q06015. http://dx.doi.org/10.1029/2012GC004096.

Wu, H., Zhang, S., Jiang, G., Hinnov, L., Yang, T., Li, H., Wan, X., Wang, C., 2013. Astrochronology of the Early Turonian–Early Campanian terrestrial succession in the Songliao Basin, northeastern China and its implications for long-period behavior of the Solar System. Palaeogeogr. Palaeoclimatol. Palaeoecol. 385, 55–70.

Zachos, J.C., McCarren, H., Murphy, B., Röhl, U., Westerhold, T., 2010. Tempo and scale of late Paleocene and early Eocene carbon isotope cycles: implications for the origin of hyperthermals. Earth Planet. Sci. Lett. 299 (1–2), 242–249. http://dx.doi.org/10.1016/j.epsl.2010.09.004.

Zeeden, C., Meyers, S.R., Lourens, L.J., Hilgen, F.J., 2015. Testing astronomically tuned age models. Paleoceanography 30, 369–383. http://dx.doi.org/10.1002/2014PA002762.

Zheng, X.-Y., Jenkyns, H.C., Gale, A.S., Ward, D.J., Henderson, G.M., 2013. Changing ocean circulation and hydrothermal inputs during Ocean Anoxic Event 2 (Cenomanian–Turonian): evidence from Nd-isotopes in the European shelf sea. Earth Planet. Sci. Lett. 375, 338–348. http://dx.doi.org/10.1016/j.epsl.2013.05.053.